Material Properties for Brady Hot Springs Nevada USA from the PoroTomo project

Kurt L. Feigl and PoroTomo Team

Award Number: DE-EE0006760
Project Title: PoroTomo: Poroelastic Tomography by Adjoint Inverse Modeling of Data from Seismology, Geodesy, and Hydrology

Project Period: 1 October 2014 through ***31 December 2018*** (extended)
Principal Investigator: Kurt Feigl, Professor, feigl@wisc.edu, (608) 262 0176
Technical Contact: Kurt Feigl, Professor, feigl@wisc.edu, (608) 262 0176
Report Submitted by: Kurt Feigl, Professor, feigl@wisc.edu, (608) 262 0176

Date of Report Submission: 6 March 2019

Project Partners:
University of Wisconsin-Madison (UW) Dept. of Geoscience http://geoscience.wisc.edu
Temple University (TU) http://astro.temple.edu/~davatzes
University of Nevada-Reno (UNR) http://geodesy.unr.edu
Ormat Technologies, Inc. http://www.ormat.com/
Silixa Ltd. http://www.silixa.com/
Lawrence Berkeley National Laboratory (LBL) http://www.lbl.gov/
Lawrence Livermore National Laboratory**Error! Bookmark not defined.** (LLNL) https://www.llnl.gov/

Material Properties for Brady Hot Springs Nevada USA from the PoroTomo project

This report compiles the results of the PoroTomo project conducted between 1 October 2014 and 31 December 2018.

In the geothermal field at Brady Hot Springs, Nevada, subsidence occurs over an elliptical area that is ~4 km by ~1.5 km. Results from inverse modeling suggest that the deformation is a result of volumetric contraction in units with depth less than 600 m. Characterizing such structures in terms of their rock-mechanical properties is essential to successful operations of Enhanced Geothermal Systems (EGS). The goal of the PoroTomo project is to assess an integrated technology for characterizing and monitoring changes in the rock-mechanical properties of an EGS reservoir in three dimensions with fine spatial resolution.

In March 2016, the PoroTomo team deployed the integrated technology in a 1500-by-500-by-400-meter volume at Brady Hot Springs. The integrated technology analyzes data from multiple arrays of sensors, including: active seismic sources, fiber-optic cables for Distributed Acoustic Sensing (DAS) and Distributed Temperature Sensing (DTS) arranged vertically in a borehole to ~400 m depth and horizontally in a trench 8700 m in length and 0.5 m in depth, 246 three-component seismometers on the surface, three pressure sensors in observation wells, continuous geodetic measurements at three GPS stations, and seven satellite images using Synthetic Aperture Radar (SAR). The deployment consisted of four distinct time intervals ("stages"). During each measurement interval, the hydrological conditions were intentionally manipulated by modifying the rates of pumping in the injection and production wells.

To account for the mechanical behavior of both the rock and the fluids, the PoroTomo team has developed numerical models for the 3-dimensional distribution of the material properties via inverse modeling of the three data sets (seismology, geodesy, and hydrology) individually. The estimated values of the material properties are registered on a three-dimensional grid with a spacing of 25 meters between nodes. The results agree on the following points. The material is unconsolidated and/or fractured, especially in the shallow layers. The structural trends follow the fault system in strike and dip. The geodetic measurements favor the hypothesis of thermal contraction. Temporal changes in pressure, subsidence rate, and seismic amplitude are associated with changes in pumping rates during the four stages of the deployment in 2016. The modeled hydraulic conductivity is high in the damage zones surrounding the faults. All the observations are consistent with a conceptual model of highly permeable conduits along faults channeling fluids from shallow aquifers to the deep geothermal reservoir tapped by the production wells.

The PoroTomo team has completed inverse modeling of the three data sets (seismology, geodesy, and hydrology) individually, as described previously. The estimated values of the material properties are registered on a three-dimensional grid with a spacing of 25 meters between nodes. The material properties are listed in Table 1. Files containing the material properties are included in three formats: Microsoft Excel (.xlsx), Comma Separated Values (.csv), and Matlab (.mat).

ID	Material property
M00	Density from Witter et al. [kg/m^3]
M01	P-wave velocity from Matzel's sweep interferometry [m/s]
M02	S-wave velocity from Matzel's sweep interferometry [m/s]
M03	Poisson's ratio from Matzel's sweep interferometry [.]
M04	Young's modulus from Matzel's sweep interferometry [Pa]
M05	P-wave velocity from body-wave tomography geophone only [m/s]
M06	Shear-wave velocity Multiscale Analysis of Surface Waves [m/s]
M07	Quality factor Qp from Matzel's sweep interferometry [.]
M08	Quality factor Qs from Matzel's sweep interferometry [.]
M10	P-wave velocity from body-wave tomography Thurber20171123 [.]
M11	Quality factor ratio Qs/Qp Matzel sweep interferometry [.]
M12	Temperature from a HT model [degC]
M15	Siler lithology [numbered unit]
M16	Strain rates in voxels from Reinisch et al. [picostrain/s]
M23	Pressure from H-T modeling [Pa]
M24	Areal fault density (area per unit volume) [m^2/m^3]
M25	Hydraulic Conductivity from [m/s]

Table 1. Identification codes of material properties.

As shown in Figure 1, the rotated coordinate system used for PoroTomo has three axes:

- The X axis is perpendicular to the strike of the dominant fault system.
- The Y axis is parallel to the strike of the dominant fault system.
- The Z axis is positive upward with respect to a reference elevation 800 meters above the WGS84 ellipsoid.

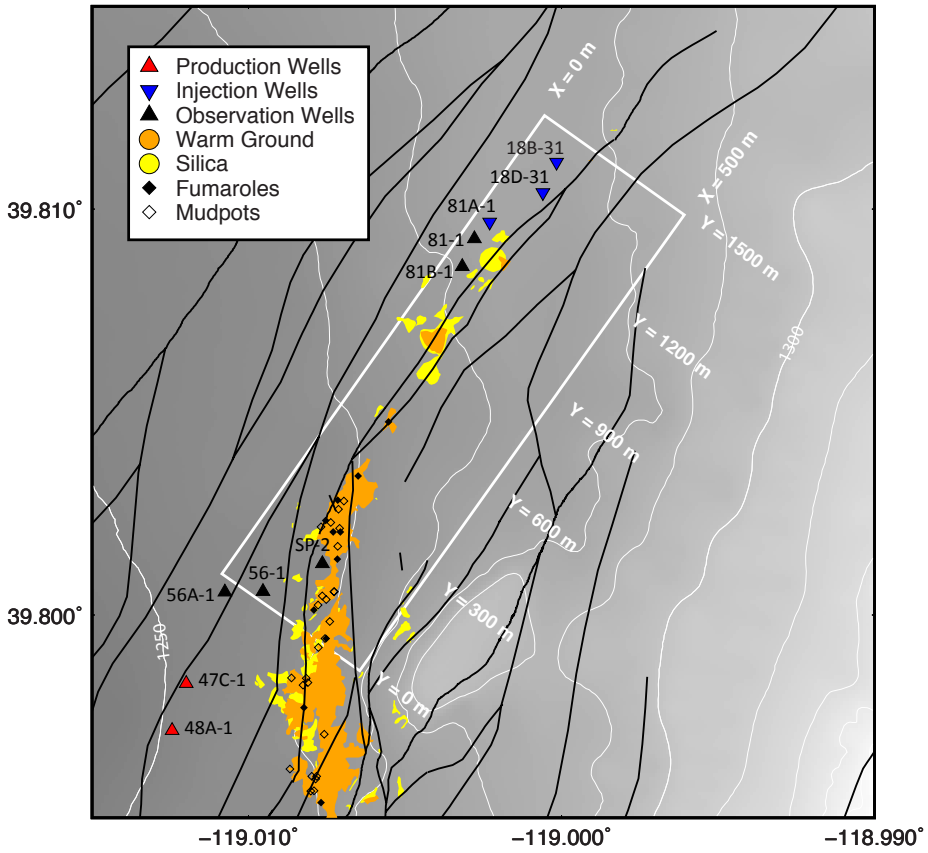

Figure 1. Map of geothermal surface features at Brady, from Parker, et al. (2018). Elevations are meters above the WGS84 ellipsoid with 10 m contour intervals. The box corresponds to the PoroTomo target area with labels of the rotated PoroTomo coordinate system.

Slices showing the material properties in a horizontal slices at 49 meters depth appear in **Figure 2** and **Figure 3**. Vertical slices in a plane perpendicular to the dominant strike of the fault system appear in **Figure 4.** Vertical slices in a plane parallel to the dominant strike of the fault system appear in **Figure 5**. Image files showing each of these slices are included in two formats: Joint Photographic Experts Group (**`.jpg`**) and Portable Document Format (**`.pdf`**). The files are named according the material property and the normal to the name of the slice. For example, the file named **`M24_FaultAreaPerUnitVolume_Siler_faults_YnormY01200m.pdf`** shows a vertical slice through the model of the fault area per unit volume on a plane normal to the strike of the fault system in PDF format. The image files are grouped by orientation (Xnorm, Ynorm, Znorm) and format (jpg or pdf) into archive (zip) files:

`XnormJPG.zip`
`XnormPDF.zip`
`YnormJPG.zip`
`YnormPDF.zip`
`ZnormJPG.zip`
`ZnormPDF.zip`

The results agree on the following points. The material is unconsolidated and/or fractured, especially in the shallow layers. The structural trends follow the fault system in strike and dip. The geodetic measurements favor the hypothesis of thermal contraction. Temporal changes in pressure, subsidence rate, and seismic amplitude are associated with changes in pumping rates during the four stages of the deployment in 2016. The modeled hydraulic conductivity is high in fault damage zones. All the observations are consistent with the conceptual model: highly permeable conduits along faults channel fluids from shallow aquifers to the deep geothermal reservoir tapped by the production wells.

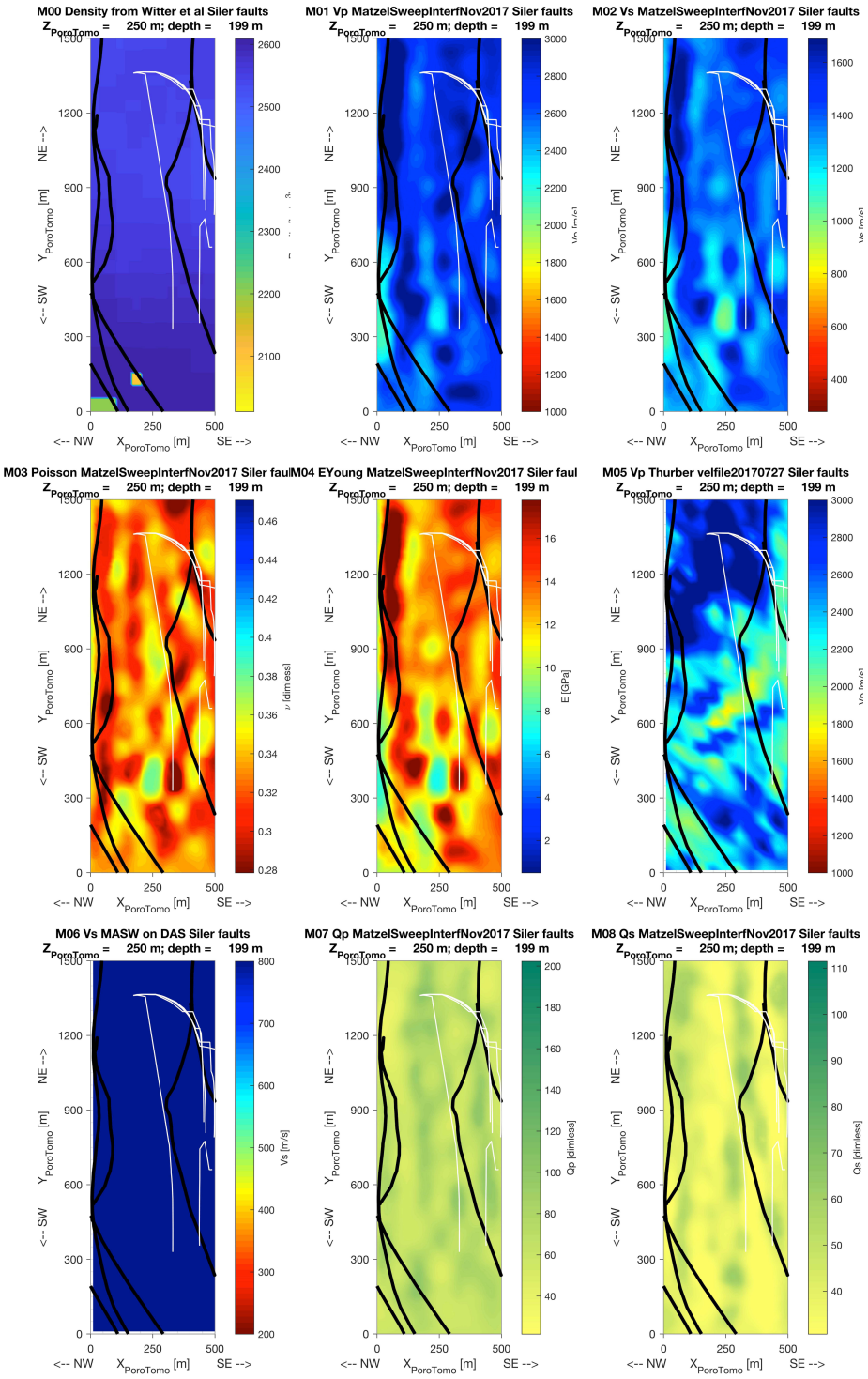

Figure 2. *Horizontal slices showing material properties at a depth of 49 m below the mean elevation of the surface. Faults (black lines) are from Siler et al. 2016. Coordinates are in the rotated PoroTomo coordinate system. Models of material properties are identified in Table 1.*

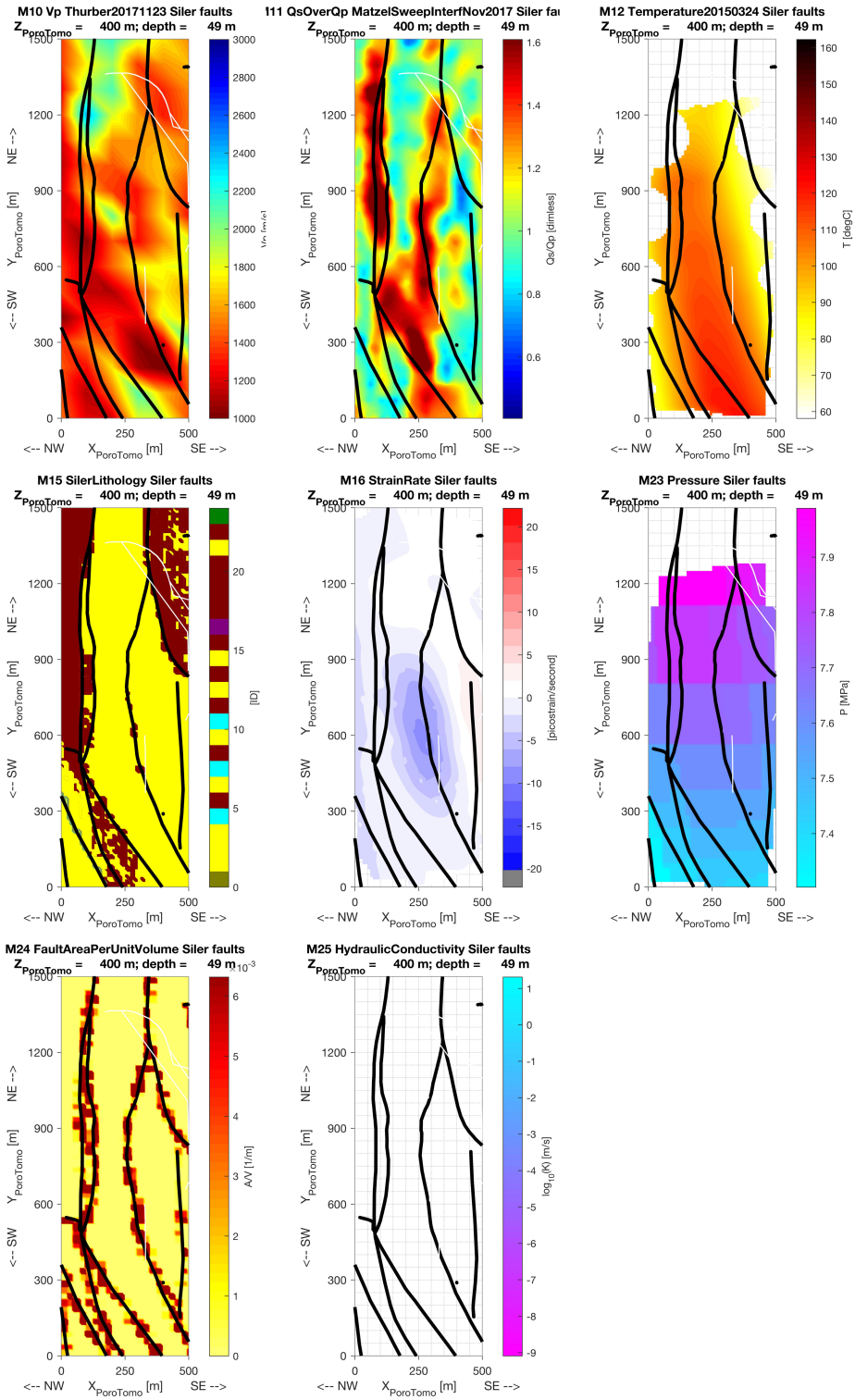

Figure 3. *Horizontal slices showing material properties at a depth of 49 m below the mean elevation of the surface. Faults (black lines) are from Siler et al. 2016. Coordinates are in the rotated PoroTomo coordinate system. Models of material properties are identified in*

.

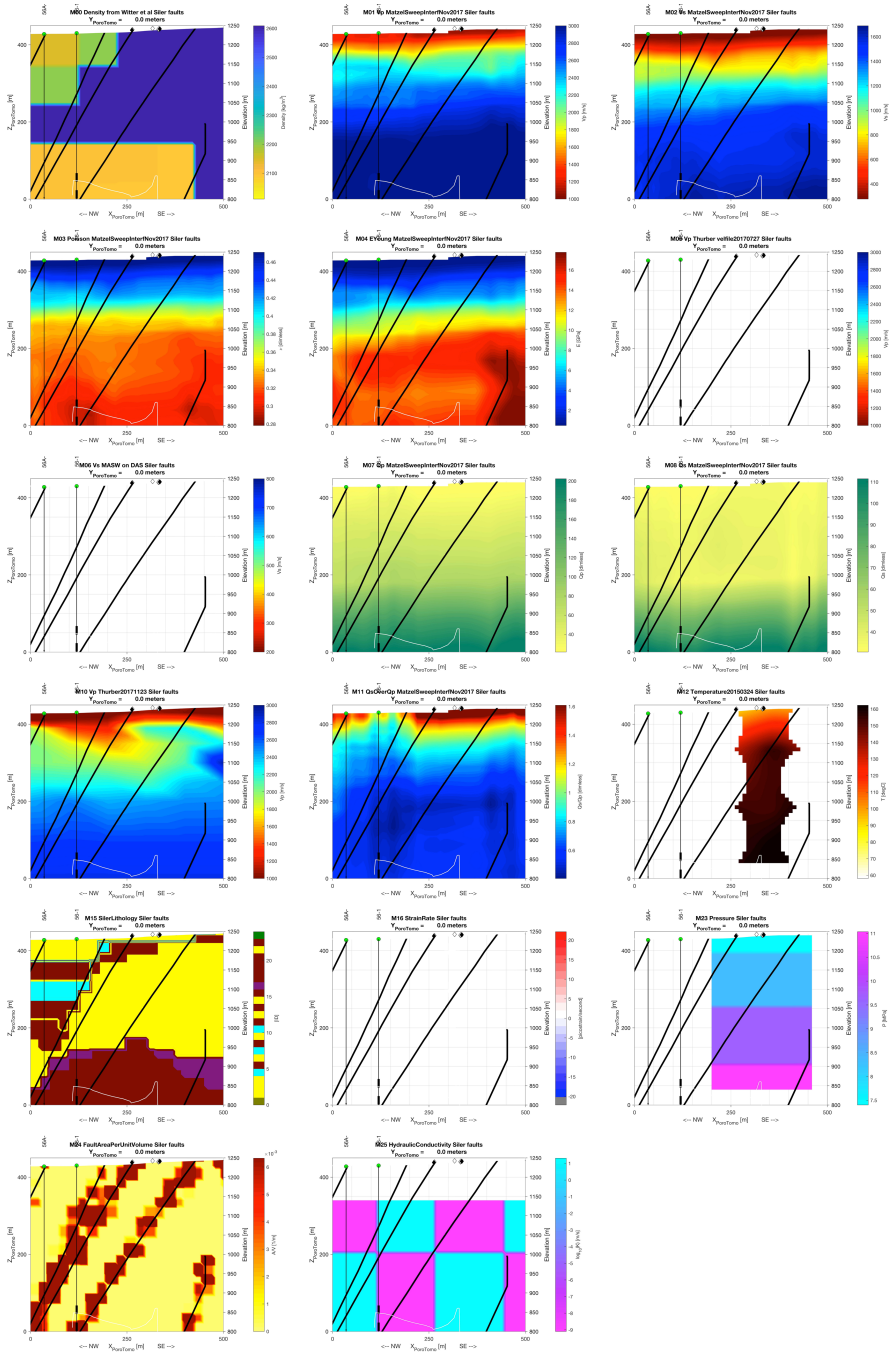

Figure 4. Vertical slices showing material properties in a plane perpendicular to the dominant strike of the normal fault system.. Faults (black lines) are from Siler et al. 2016. Coordinates are in the rotated PoroTomo coordinate system. Models of material properties are identified in Table 1.

.

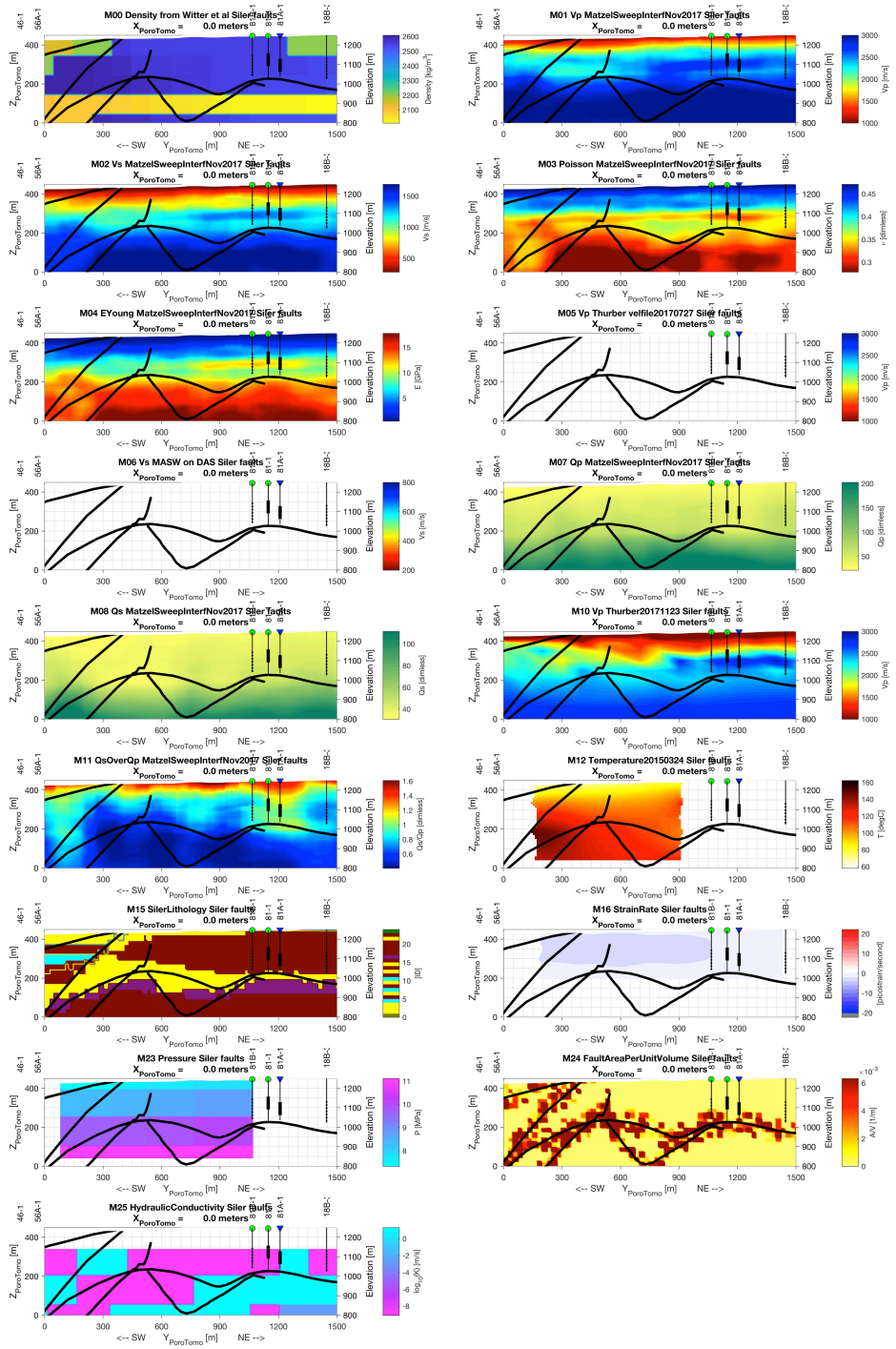

Figure 5. *Vertical slice showing material properties in a plane parallel to the dominant strike of the normal fault system.. Faults (black lines) are from Siler et al. 2016. Coordinates are in the rotated PoroTomo coordinate system. Models of material properties are identified in Table 1.*

Details on estimated values of material properties

M00 Density from Witter et al. [kg/m^3]

Model M00 shows density in kilograms per cubic meter from the study by Witter et al. (2016), for which the abstract follows. Values have been interpolated to the PoroTomo mesh with 25-meter spacing between points.

Witter, J. B., D. L. Siler, J. E. Faulds, and N. H. Hinz (2016), 3D geophysical inversion modeling of gravity data to test the 3D geologic model of the Bradys geothermal area, Nevada, USA, Geotherm Energy, 4, 14. http://dx.doi.org/10.1186/s40517-016-0056-6

Three-dimensional geophysical inversion modeling of gravity data has been performed to test the validity of a 3D geologic model constructed for the Bradys geothermal area. Geophysical modeling was implemented in three different ways: (1) fully unconstrained (i.e., no geologic data included); (2) constrained by the 3D geologic model using homogeneous rock unit densities, and (3) constrained by the 3D geologic model using heterogeneous rock unit densities. We show that the existing 3D geologic model of the Bradys area is broadly consistent with the gravity data. At a more detailed level, however, our analysis suggests that some adjustments to the Bradys 3D geologic model would improve agreement between the observed gravity and the calculated gravity response. The results of the geophysical inversion modeling are important as they serve as a guide to show where and how the boundaries of the 3D geologic model may need to be adjusted to address density excesses and deficiencies. A 3D geologic model that has been independently tested prior to drilling (using a method such as that described in this paper) will be more robust and have less uncertainty than those which have not been tested. Such an approach will facilitate a reduction in drilling risk, lead to more successful drilling programs, and provide valuable geologic input to improve the accuracy of reservoir models.

1 P-wave velocity from Matzel's sweep interferometry [m/s]

Model M01 contains the P-wave velocity in meters per second estimated using “sweep interferometry” as described by Matzel et al. (2017a; 2017b):

Matzel, E., X. Zeng, C. Thurber, Y. Luo, C. Morency, and PoroTomo_Team (2017), Seismic Interferometry Using the Dense Array at the Brady Geothermal Field (abstract SGP-TR-212), paper presented at Stanford Geothermal Workshop, Stanford University.

Matzel, E., X. Zeng, C. Thurber, C. Morency, K. Feigl, and PoroTomo_Team (2017), Using Virtual Earthquakes to Characterize the Material Properties of the Brady Hot Springs, Nevada paper presented at Geothermal Research Council Transactions, Salt Lake City. https://www.osti.gov/scitech/servlets/purl/1399706.

2 S-wave velocity from Matzel's sweep interferometry [m/s]

Model M02 contains the shear-wave velocity in meters per second estimated using “sweep interferometry” as described by Matzel et al. (2017a; 2017b).

3 Poisson's ratio from Matzel's sweep interferometry [.]

Model M03 contains the (dimensionless) Poisson ratio calculated from the ratio of P-wave velocity Vp to S-wave velocity Vs, each estimated using “sweep interferometry” as described by Matzel et al. (2017a; 2017b). The relevant formula is:

```
%https://en.wikipedia.org/wiki/Elastic_modulus
VpOverVs = Vp ./ Vs;
Poisson = 0.5*((VpOverVs.^2) - 2)./((VpOverVs.^2)-1);
```

4 Young's modulus from Matzel's sweep interferometry [Pa]

Model M04 contains the Young's modulus calculated from the P-wave velocity Vp and the S-wave velocity Vs, each estimated using "sweep interferometry" as described by Matzel et al. (2017a; 2017b). The density is from the study by Witter et al. (2016). The relevant formulae are:

```
% https://en.wikipedia.org/wiki/P-wave_modulus
% In linear elasticity, the P-wave modulus Mp, also
% known as the longitudinal modulus or the constrained modulus, is one of
% the elastic moduli available to describe isotropic homogeneous materials.
Mp = Density_kg_per_m3 .* (Vp).^2;
% Young's modulus
EYoung  = Mp .* (1 + Poisson) .* (1 - 2*Poisson) ./ (1 - Poisson);
```

M05 P-wave velocity from body-wave tomography geophone only [m/s]

Model M05 contains the P-wave velocity in meters per second estimated using body-wave tomography. This preliminary result used a set of travel times picked from the seismograms recorded by Fairfield Nodal geophones only. In other words, no data from distributed acoustic sensing (DAS) were included in this inversion.

M06 Shear-wave velocity Multiscale Analysis of Surface Waves [m/s]

Model M06 contains shear-wave velocity in meters per second, as estimated by Zeng et al. (2017b):

Zeng, X., C. H. Thurber, H. F. Wang, D. Fratta, and Porotomo_Team (2017b), 3D shear wave velocity structure revealed with ambient noise tomography on a DAS array (abstract #S33F-06), in Fall Meeting Amer. Geophys. Un., edited, New Orleans.

M07 Quality factor Qp from Matzel's sweep interferometry [.]

Model M07 contains the quality factor Q for P waves estimated using "sweep interferometry" as described by Matzel et al. (2017a; 2017b). Lower values of Q imply more attenuation of seismic waves.

M08 Quality factor Qs from Matzel's sweep interferometry [.]

Model M08 contains the quality factor Q for S waves estimated using "sweep interferometry" as described by Matzel et al. (2017a; 2017b). Lower values of Q imply more attenuation of seismic waves.

M10 P-wave velocity from body-wave tomography Thurber20171123 [m/s]

Model M10 contains the P-wave velocity in meters per second estimated using body-wave tomography, as described by Parker et al., (2018), for which the abstract follows. This inversion contains travel times picked from Fairfield Nodal geophones, horizontal DAS, and vertical DAS.

M11 Quality factor ratio Qs/Qp Matzel sweep interferometry [.]

Model M11 contains the ratio of the quality factor Qs for S waves to the quality factor Qp for P waves, each estimated using "sweep interferometry" as described by Matzel et al. (2017a; 2017b). Qualitatively, lower values of Qs/Qp may be interpreted as material that has lower fluid saturation and/or is more compact.

M12 Temperature from a HT model [degC]

Model M12 contains temperature in degrees Celsius as calculated in a simulation. The calculation couples the hydrologic flow (Darcy's Law) with simple thermodynamics. The epoch of validity is 24 March 2015. Values have been interpolated from a data set that is available on GDR as: https://dx.doi.org/10.15121/1369075.

M15 Siler lithology [numbered unit]

Model M15 contains lithologic units as identified in the geologic model of Siler et al. (2016), for which the abstract follows.

Siler, D. L., N. H. Hinz, J. E. Faulds, and J. Queen (2016), 3D analysis of geothermal fluid flow favorability: Brady's, Nevada, USA, paper presented at PROCEEDINGS, 41st Workshop on Geothermal Reservoir Engineering Stanford University, Stanford, California, February 22-24, 2016 SGP-TR-209.
https://pangea.stanford.edu/ERE/pdf/IGAstandard/SGW/2016/Siler.pdf

Geothermal circulation requires heat, permeability and fluids. Fracture permeability along discrete fault zones provides the pathways for fluid convection. Within individual faults, however, fluid flow zones can have variable character, size, and spatial distribution, representing a significant challenge to exploration and evaluation of geothermal resources. A comprehensive and validated methodology for quantitatively identifying the character, extent, and location of most likely fluid upflow zones within a resource area does not exist. Here, we present a methodology for evaluating favorability for geothermal fluid flow in 3D, an application of this technique to the Brady's geothermal system, Nevada, USA, and a preliminary evaluation of the results based on data from the production field. A variety of data types, including 2D seismic reflection data, downhole lithologic data, and geologic map data are integrated in 3D space in order to develop a 3D geologic model of the Brady's geothermal system. From this geologic model, the stress state of modeled faults, the density of fault intersections, and the inferred fluid flow characteristics of the various stratigraphic intervals are evaluated as proxies for permeability and geothermal fluid flow. Integration of these results with temperature data reveals locations within the geothermal field where the collocation of probable fracture permeability and high temperatures indicates a high likelihood for hosting geothermal fluid circulation. These results are consistent with the locations of injection, production, and non-productive wells within the Brady's field. Validation of these results with data from the well field suggests that these techniques do indeed shed light on specific details of the fluid flow systematics in geothermal systems. Though Brady's is a relatively data-rich system, this methodology can be adapted and applied to exploration and resource assessment not only in mature production fields, but also in blind, greenfield and otherwise data- poor geothermal areas.

Lithologic units are coded using the following identification numbers. The color table groups similar lithologies together.

```
ID, Symbol, Lithology
1,  Q, Quaternary sediments, undifferentiated
2,  Tsy, Tertiary sediments
3,  Tsl6, Tertiary lacustrine sediments
4,  Tsl5, Tertiary lacustrine sediments
5,  Tls3, Tertiary limestone
6,  Tbo7, Tertiary basalt flows
7,  Tsl4, Tertiary lacustrine sediments
8,  Tls2, Tertiary limestone
9,  Tbo6, Tertiary basalt flows
10,  Tsl3, Tertiary lacustrine sediments
11,  Tls1, Tertiary limestone
12,  Tbo5, Tertiary basalt flows
13,  Tsl2, Tertiary lacustrine sediments
14,  Tbo4, Tertiary basalt flows
15,  Tsl1, Tertiary lacustrine sediments
16,  Tbo3, Tertiary basalt flows
17,  Tpd, Tertiary Porphrytic (hornblende-biotite)
     dacite to rhyodacite flows and domes
```

```
18,  Tbo2, Tertiary basalt flows
19,  Tlr, Tertiary rhyolite lavas and lesser tuffs
20,  Tbo1, Tertiary basalt flows
21,  Tda, Tertiary andesite to dacite lavas
22,  Tslo, Tertiary lacustrine sediments
23,  Trt, Tertiary (Oligocene) ash-flow tuffs
24,  Mzu, Mesozoic undifferentiated
```

16 Strain rates in voxels from Reinisch et al. [1/s]

Model M16 shows the volumetric strain rate estimated from InSAR data in a model of thermal contraction, as described by Reinisch et al. (2018):

> Reinisch, E. C., M. Cardiff, and K. L. Feigl (2018), Characterizing Volumetric Strain at Brady Hot Springs, Nevada, USA Using Geodetic Data, Numerical Models, and Prior Information, *Geophys. J. Int.*, 1501–1513. http://dx.doi.org/10.1093/gji/ggy347

23 Pressure from H-T modeling [Pa]

Model M23 contains fluid pressure in Pa as calculated in a simulation. The calculation couples the hydrologic flow (Darcy's Law) with simple thermodynamics. The epoch of validity is 24 March 2015. Values have been interpolated from a data set that is available on GDR as: https://dx.doi.org/10.15121/1369075.

24 Areal fault density (area per unit volume) [m^2/m^3]

Model M24 contains the surface area of faults per unit volume as identified in the geologic model of Siler et al. (2016). Starting with 3-dimensional coordinates of each fault, we found the best-fitting plane and defined a mesh surface using a Delaunay triangulation. We then calculated the locus of points defined by the intersection of the fault surface with each of the six faces of a cube with volume $(25\ m)^3$. The surface area of the polygon is then normalized by the volume of the cube to give the fault density in square meters per cubic meter.

25 Hydraulic Conductivity [m/s]

Model M25 shows hydraulic conductivity in meters per second as estimated from hydro-geologic modeling by Jeremy Patterson and Mike Cardiff. The details are described in Patterson's Master's Thesis, entitled, "Understanding Constraints on Geothermal Sustainability Through Reservoir Characterization at Brady Geothermal Field, Nevada."

References

Matzel, Eric, Xiangfang Zeng, Clifford Thurber, Yan Luo, Christina Morency, and PoroTomo Team (2017a). Seismic Interferometry Using the Dense Array at the Brady Geothermal Field, PROCEEDINGS, 42nd Workshop on Geothermal Reservoir Engineering, Stanford University, Stanford, California, February 13-15, 2017, 3-6.

Matzel, E., X. Zeng, C. Thurber, C. Morency, K. Feigl, and PoroTomo_Team (2017b), Using Virtual Earthquakes to Characterize the Material Properties of the Brady Hot Springs, Nevada paper presented at Geothermal Research Council Transactions, Salt Lake City. https://www.osti.gov/scitech/servlets/purl/1399706.

Parker, L. M., C. H. Thurber, X. Zeng, N. E. Lord, D. Fratta, H. F. Wang, M. C. Robertson, A. M. Thomas, M. S. Karplus, A. Nayak, and K. L. Feigl (2018). Active-source seismic tomography at the Brady Geothermal Field, Nevada, with dense nodal and fiber-optic seismic arrays. *Seismological Research Letters*, **89**, 1629-1640, doi:10.1785/0220180085.

Patterson, J., M. Cardiff, T. Coleman, H. Wang, K. Feigl, J. Akerley, and P. Spielman (2017). Geothermal reservoir characterization using distributed temperature sensing at Brady Geothermal Field, Nevada. *Leading Edge*, **36**(12), 1024a1–1024a7. doi: 10.1190/tle36121024a1.1.

Patterson, Jeremy, Michael A. Cardiff, David Lim, Thomas Coleman, Herb F. Wang, Kurt L. Feigl, and PoroTomo Team (2017). Characterization of Hydrologic and Thermal Properties at Brady Geothermal Field, NV. presented at American Geophysical Union Fall Meeting 2017, New Orleans.

Patterson, Jeremy (2018), Understanding Constraints on Geothermal Sustainability Through Reservoir Characterization at Brady Geothermal Field, Nevada (Master's Thesis), University of Wisconsin, Madison, 129 p.

Reinisch, Elena C., Michael Cardiff, Kurt L. Feigl (2016). Graph theory for analyzing pair-wise data: application to geophysical model parameters estimated from interferometric synthetic aperture radar data at Okmok volcano, Alaska. *Journal of Geodesy*, **91**(1), 9-24. http://dx.doi.org/10.1007/s00190-016-0934-5.

Reinisch, Elena C., Kurt L. Feigl, Michael A. Cardiff, Christina Morency, Corné Kreemer, John Akerley, and PoroTomo Team (2017). Characterizing Volumetric Strain at Brady Hot Springs, Nevada, USA Using Geodetic Data, Numerical Models, and Prior Information. presented at American Geophysical Union Fall Meeting 2017, New Orleans.

Reinisch, E. C., Cardiff, M., & Feigl, K. L. (2018). Characterizing Volumetric Strain at Brady Hot Springs, Nevada, USA Using Geodetic Data, Numerical Models, and Prior Information. *Geophysical Journal International*, **215**(2), 1501–1513. doi:10.1093/gji/ggy347

Siler, D. L., and J. E. Faulds (2013). Three-Dimensional Geothermal Fairway Mapping: Examples From the Western Great Basin, USA. *GRC Transactions*, **42**, 327-332.

Siler, D. L., N. H. Hinz, J. E. Faulds, and J. Queen (2016). 3D analysis of geothermal fluid flow favorability: Brady's, Nevada, USA, *PROCEEDINGS*, 41st Workshop on Geothermal Reservoir Engineering Stanford University, Stanford, California, February 22-24, 2016, 10 p. https://pangea.stanford.edu/ERE/db/GeoConf/papers/SGW/2016/Siler.pdf

Thurber, Clifford H., Lesley Parker, Peng Li, Dante Fratta, Xiangfang Zeng, Kurt L. Feigl, Esra Ak, Neal Lord, and PoroTomo Team (2017). Active-Source Seismic Tomography at Bradys Geothermal Field, Nevada, with Dense Nodal and Fiber-Optic Seismic Arrays. presented at American Geophysical Union Fall Meeting 2017, New Orleans.

Witter, J. B., Siler, D. L., Faulds, J. E., and Hinz, N. H. (2016). 3D geophysical inversion modeling of gravity data to test the 3D geologic model of the Bradys geothermal area, Nevada, USA. *Geothermal Energy*, **4**(14), 21 p. https://doi.org/10.1186/s40517-016-0056-6

Zeng, Xiangfang, Clifford H. Thurber, Yan Luo, Eric Matzel, and PoroTomo Team (2016). High-resolution shallow structure revealed with ambient noise tomography on a dense array. presented at American Geophysical Union Fall Meeting 2016, San Francisco.

Zeng, X., C.Thurber, H. Wang, D. Fratta, E. Matzel, and The PoroTomo Team (2017). High-resolution Shallow Structure Revealed with Ambient Noise Tomography on a Dense Array. *PROCEEDINGS,* 42nd Workshop on Geothermal Reservoir Engineering, Stanford University, Stanford, California, February 13-15, 2017, 5 p.

Zeng, X., C. Lancelle, C. Thurber, D. Fratta, H. Wang, N. Lord, A. Chalari, and A. Clarke (2017). Properties of noise cross-correlation functions obtained from a distributed acoustic sensing array at Garner Valley, California. *Bulletin of the Seismological Society of America*, **107**(2), 603-610. https://doi.org/10.1785/0120160168.

Zeng, Xiangfang, Clifford H. Thurber, Herb F. Wang, Dante Fratta, and Porotomo Team (2017). 3D shear wave velocity structure revealed with ambient noise tomography on a DAS array. presented at American Geophysical Union Fall Meeting 2017, New Orleans.